Advancements in Drone-Based (UAV) Ground Penetrating Radar for Accurate Boundary Mapping between Disturbed Clayey Soil and Natural Rock

Michael Frid and Vladimir Frid *

Posted Date: 14 January 2024

doi: 10.20944/preprints202401.1034.v1

Keywords: ground penetrating radar; drone technology; geophysical prospecting; civil engineering

Article

Advancements in Drone-based (UAV) Ground Penetrating Radar for Accurate Boundary Mapping between Disturbed Clayey Soil and Natural Rock

Michael Frid [1] and Vladimir Frid [2*]

[1] Geoscope Ltd, Rosmarin 17, Beer Sheva, 8465041, Israel, geoscopegpr@gmail.com
[2] Sami Shamoon College of Engineering, Jabotinsky 84, Ashdod 77245, Israel
* Correspondence: vladimirf@ac.sce.ac.il

Abstract: The main goal of the research is to assess the effectiveness of aerial ground-penetrating radar (GPR) in delineating boundaries between disturbed clayey ground and rock formations along the old Wadi. The study also tackles technical challenges associated with drone-based GPR applications in urban open areas, considering geological heterogeneity, topographic variations, and environmental conditions. The potential of using drone-based GPR equipped with an unshielded dipole antenna as a transformative tool in geospatial analysis was demonstrated. The research encompasses academic insights and field borehole drilling experiments to validate the accuracy and reliability of drone-based GPR data in real-world scenarios. Anticipated contributions include advancements in understanding drone-based GPR technology for mapping disturbed soil boundaries in foundation engineering applications and other relevant areas and recommendations for optimizing its performance in challenging terrains.

Keywords: ground penetrating radar; drone technology; geophysical prospecting; civil engineering

1. Introduction

Accurate mapping of boundaries between disturbed ground and natural rock or soil is critical for advancing foundation engineering practices [1–3]. Conventional surveying methods, including local 1D borehole drilling and manual 2D geophysical surveys (e.g., Electrical resistivity tomography), face limitations in coverage, cost, and time efficiency, especially in challenging terrains [1,4]. Overcoming these challenges requires innovative techniques like ground-penetrating radar (GPR) to understand subsurface structures comprehensively. Beyond foundation engineering, in agriculture, traditional land GPR has already found applications in monitoring soil water content during irrigation in clay-disturbed soils [5] and mapping nonlinear boundaries between covering clayey soil and natural soil for agricultural purposes [6]. For example, Guo et al. [7] utilized land-based GPR to study the 3D sedimentary architecture of recent sediments in the Yungang braided river study area in Datong (China), emphasizing the need to characterize unstable, disturbed ground quantitatively.

Environmental applications also include using land-based GPR in prospecting alluvial karst and structures associated with subsidence areas [8]. Sass et al. [4] applied ground-based GPR to gain knowledge about the thickness and internal structure of the Öschingen landslide in Germany, detecting near-surface sediment structures despite signal attenuation and reflections. In transportation infrastructure assessment, the GPR unit attached to a railway vehicle was used to assess the condition of Croatia's old railway underground infrastructure [9,10]. The numerous applications of GPR for road pavement assessment were reviewed in [11]. The railway/highway vehicle-based GPR studies are held above the ground at a fixed distance, mapping underground infrastructure, including pavement thickness, disturbed soil, and gravel inventories.

However, ground-based GPR is limited to a few measurement lines in relatively flat and accessible areas convenient for traditional land GPR measurement.

 doi:10.20944/preprints202401.1034.v1

On the other hand, Airborne ground-penetrating radar (GPR) emerges as a cutting-edge technology, utilizing electromagnetic waves to penetrate the subsurface and capture detailed geological information [12]. In contrast to traditional ground-based GPR, drone-based GPR offers several advantages over conventional ground-based methods [13]. Unmanned aerial vehicles (UAVs) equipped with GPR sensors can rapidly and non-invasively cover large and unacceptable areas, offering a three- and even four-dimensional perspective of the subsurface boundaries with their geotechnical properties and achieving heightened spatial resolution [14].

Additionally, what sets drone-based GPR apart is the Real-Time Kinematic (RTK) GPS positioning. That enables precise survey paths to be repeated, opening new opportunities for 4D data acquisitions [15]. The UAV-mounted GPR system, equipped with advanced signal processing techniques such as cross-correlation-based background subtraction and interference suppression [16,17], ensures accurate detection of underground targets. Geotechnical properties such as soil moisture mapping [18] and field-scale soil electrical conductivity mapping [19] can be achieved using drone-borne GPR.

This technology is beneficial in regions with limited accessibility, such as hill slopes prone to landslides or areas affected by colliery waste. Ruols et al. [20] successfully recorded a significant 3D dataset using drone-borne controlled-source electromagnetic (CSEM) systems over alpine glaciers, showcasing the feasibility of obtaining intricate imagery of the immediate subsurface in challenging terrains. Vergnano et al. [21] also applied drone-borne GPR with a 900 MHz antenna for snow cover depth mapping in the Alpine regions. Concluding that drone technology is ready to support GPR-based applications at high altitudes and mapping the proper surface under snow cover.

Saponaro et al. [22] exemplified the utility of drone-mounted GPR in guiding and optimizing mining operations. By mounting two 120 MHz GPR antennas on a drone, they successfully mapped structural discontinuities within local geological materials in a quarry excavation area in Falconara Albanese, Italy. This application demonstrates the adaptability of drone-based GPR for specific geological investigations. Edemsky et al. [23] conducted experiments in challenging clay soils, revealing characteristic objects in the upper subsurface environment using airborne GPR. However, the challenges of using GPR in clayey soil, where electromagnetic waves rapidly decay, are acknowledged [23]. This difficulty is manageable, as Cheng et al. [6] demonstrated when using land GPR for mapping disturbed clayey layers in agricultural fields.

Similar to [21], our study uses drone-based GPR to map disturbed clayey ground depth. Despite the challenges, Edemsky et al. [23] highlighted penetrating clayey soil with aerial GPR due to fast wave decay. Experiences in land GPR applications, such as [6] mapping of disturbed clayey layers in agricultural fields, suggest potential avenues for success.

The primary objective of our research is to investigate the efficacy of aerial ground-penetrating radar in mapping boundaries between disturbed clayey ground and the rock formation based on the old Wadi and showcasing its potential as a transformative tool in geospatial analysis.

The study also addresses technical challenges associated with drone-based GPR applications in urban open areas, considering geological heterogeneity, topographic variations, and environmental conditions. The scope encompasses academic information and borehole drilling experiments in the field to validate the accuracy and reliability of UAV-based GPR data in a real-world scenario. Anticipated contributions of this research include advancements in the understanding of drone-based GPR technology in disturbed soil boundary mapping for foundation engineering applications and in other areas where this is required and recommendations for optimizing its performance in challenging terrains.

2. The site under study

The construction site under study is located in Beer-Sheva city on the northern edge of the Negev desert, approximately 115 kilometers southeast of Tel Aviv and 120 kilometers southwest of Jerusalem. The town is positioned along the primary route from the central and northern parts of the country to Eilat in the far south (Figure 1a). Specifically, the site is located in the western part of the city (Figure 1b) within the boundaries of old Wadi, filled by disturbed clayey soil during the

Preprints (www.preprints.org) | NOT PEER-REVIEWED | Posted: 14 January 2024 doi:10.20944/preprints202401.1034.v1

Children's Park construction (Figure 1c). The filling soil is classified as low plastic inorganic clay up to silty clay (CL/ML indexes following the Unified Soil Classification System [24]). This soil is a matrix for carbonate pebble-size material overlaying calcareous sandstone from the Pliocene period (Figure 1d). A drilling survey, intended to reach a depth of 15 meters, faced essential challenges and was prematurely halted at 5 meters. A robust underground water stream necessitated this cessation and the collapse of the disturbed clayey ground, vividly illustrated in Figure 2. Antecedent government topographic data for the region indicated the presence of natural rock or soil surfaces at depths ranging from 8 to 15 meters, lacking precise details.

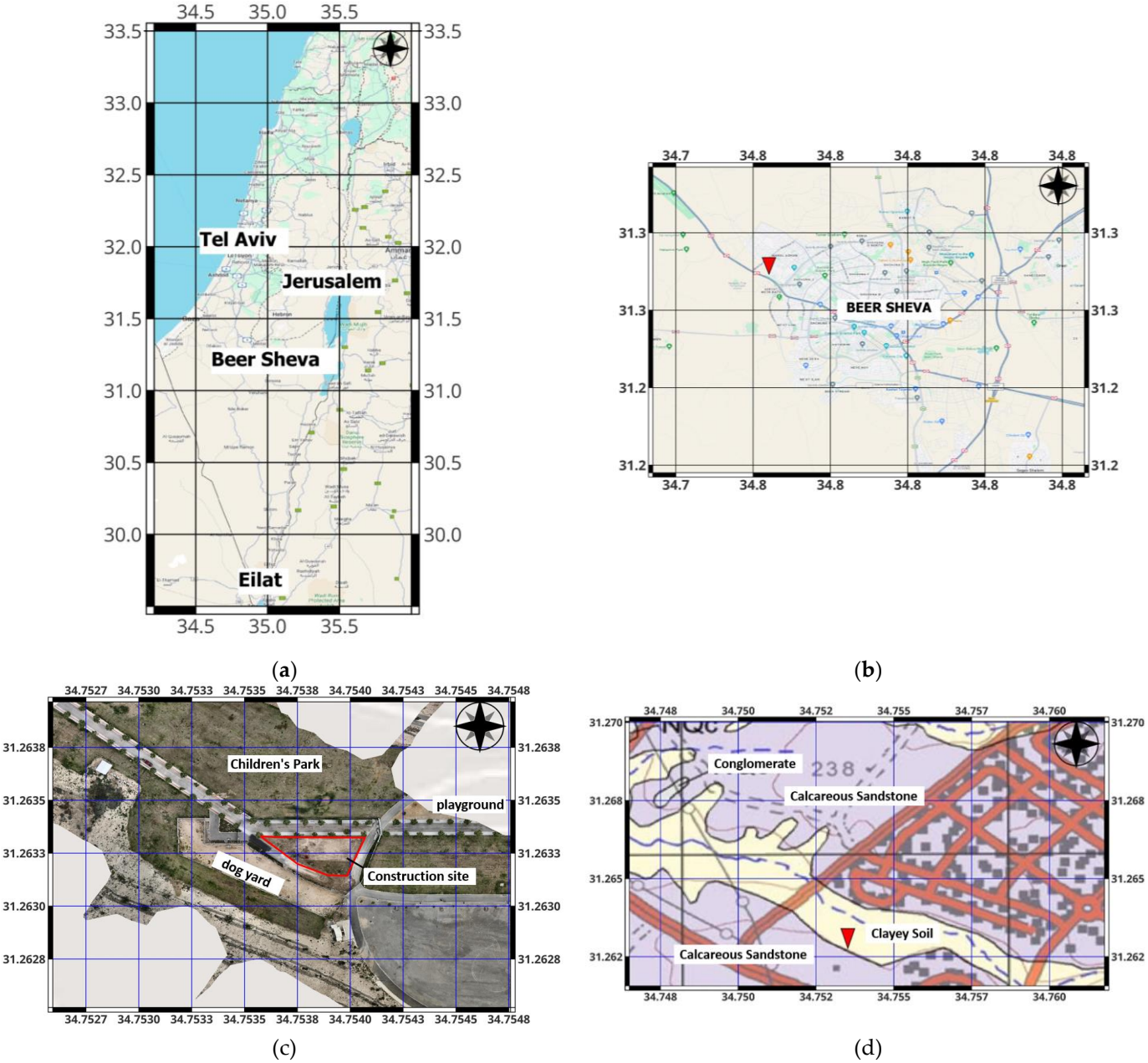

Figure 1. The maps of the construction site under study. **(a)** The zoom-out map of Israel, **(b)** The map of Beer Sheva city with a superimposed red triangle indicating the location of the site under study, **(c)** The orthophoto of the Children's Park with the construction site under study marked with red, made right before the survey, **(d)** The zoom-in fragment of the geological map of the region [25] with a superimposed red triangle indicating the location of the site under study.

 doi:10.20944/preprints202401.1034.v1

(a) (b) (c)

Figure 2. The photographs of the drilling campaign. **(a)** The drilling machine used for the campaign aborted midway, **(b)** The closer view around the drilling borehole reveals a distributed soil (filling) composition, primarily consisting of approximately 90% CL/ML matrix [24] and 10% random concentrations of white chalk pebbles, **(c)** Zoom inside the drilling borehole, depicting the presence of water at a depth of 5 meters and evident collapse in the pit's sides around 4 meters depth.

3. Materials and Methods

A drone-based GPR system comprises integral components, each playing a crucial role in ensuring the accuracy and functionality of the technology. The fundamental component at the core of this system is the GPR unit manufactured by RADAR Systems, Inc. (RADAR SYSTEMS Inc., Riga, Latvia). This single-unit GPR includes the radar transmitter and receiver antennas, which emit electromagnetic waves into the ground and capture the reflected signals. The selection of antennas is a critical consideration, tailored to the specific application, considering factors such as the desired penetration depth and resolution.

The amalgamation of GPR technology with drone technology for foundation engineering surveys signifies a synergistic alliance between aerial platforms and subsurface sensing capabilities. As depicted in Figure 3, the GPR unit is securely mounted onto the drone, positioned beneath the aircraft, with the radar antennas (the dipole antenna in the case under study). This configuration enables the drone to transport the GPR system while maintaining an optimal distance from the ground to ensure accurate data acquisition. Furthermore, Real-Time Kinematic (RTK) technology is seamlessly integrated to provide georeferencing, facilitating precise data mapping to specific geographical coordinates. The SKYHUB computer (SPH Engineering, Riga, Latvia) meticulously maintains data synchronization between the DJI M300 drone and the GPR unit, ensuring coherent and reliable information collection throughout the flight.

Several crucial specifications must be considered to attain optimal performance in the integration process. The selection of the GPR frequency is paramount as it directly influences the depth of penetration and the resolution of subsurface data. Lower frequencies provide greater depth penetration but may compromise resolution, while higher frequencies offer finer details at shallower depths [26]. The choice of the appropriate frequency band hinges on specific research objectives and the characteristics of the particular site under investigation [26,27].

 doi:10.20944/preprints202401.1034.v1

Figure 3. A DJI M-300 drone with a GPR 150 MHz dipole antenna at the bottom provides subsurface sensing capabilities up to 15 m below the surface. The Sky-Hub computer, which is positioned on the right side, is responsible for controlling automatic flight operations. At the front of the drone, a small radar (altimeter) measures the distance from the ground, maintaining a constant flight altitude of 5 meters. The survey took place around the construction site at the Children's Park in Beer-Sheva City, Israel (Figure 1c).

To address the uncertainty in geological exploration by borehole drilling and optimize subsurface penetration, a drone-based GPR system was configured with a central frequency of 150 MHz. The chosen operating bandwidth spans from 75 to 300 MHz, with a scan resolution of 512 to 1024 samples per scan. This GPR configuration aims to provide detailed insights into the subsurface composition, contributing to a comprehensive understanding of the geological structure in the construction site vicinity. Moreover, the drone's payload capacity and flight time are critical factors influencing the system's overall usability. A well-balanced drone with adequate payload capacity ensures the secure mounting of the GPR unit without compromising flight stability.

Drones present a distinctive advantage in their adeptness at efficiently covering expansive areas while effortlessly navigating urban impediments such as fences, trees, bushes, and streetlights, thereby maintaining a constant and stable flight pattern around the area of interest. Given the prevalence of high trees and fences encircling the construction site at Children's Park(Figures 1c and 3), the drone's flying altitude was restricted to 5 meters above the surface. To optimize data acquisition over the undulating terrain of the park, the selected flight path commenced at the hilltop, descending around the construction site's center, aligning with the natural surface of the hills beneath the distributed soil. Leveraging SKYHUB technology, the drone's trajectory is pre-programmed to follow a designated pattern, often comprised of parallel flight lines or a grid configuration tailored to the research objectives. These predefined patterns enable the GPR sensors to capture data across the entire survey area precisely. Figure 4 visually represents the specific flight pattern executed in the park around the areas of interest.

Preprints (www.preprints.org) | NOT PEER-REVIEWED | Posted: 14 January 2024 doi:10.20944/preprints202401.1034.v1

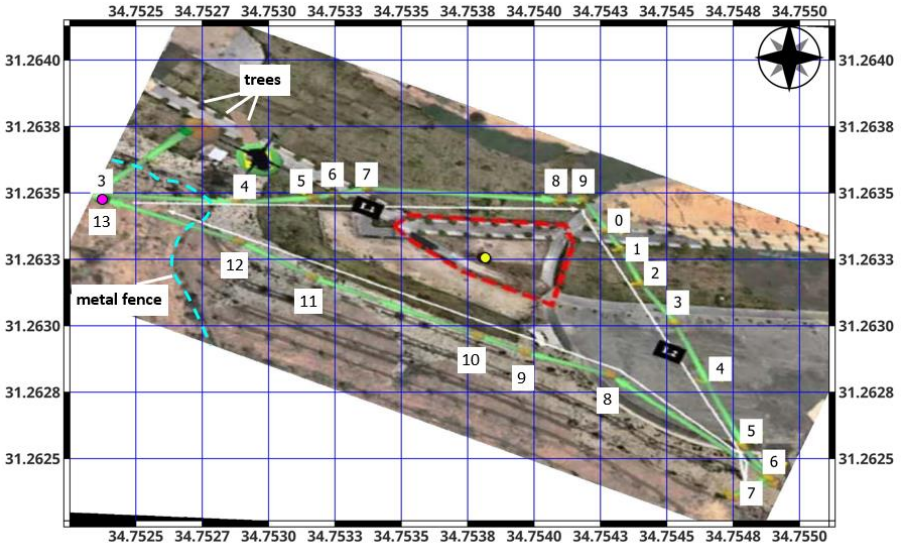

Figure 4. The Children's Park construction site (dashed red line) is enclosed by a white fence (Figure 3). The yellow point in the center marks the drilling test location (Figure 2). The drone's precise flight path begins and ends at the west corner of the hilltop (purple circle), capturing changes in the natural surface under the distributed clayey soil. Obstacles like streetlights, trees (marked with white), and a metal fence (marked with blue) are visible on the map. The numbers show the straight section of the drone flight.

The flight altitude and speed of the drone impact the flight-path design, as they affect the sensor's effective field of view. Like ground-based GPR, slow velocity scanning is preferable for underground features [26,27]; therefore, the flight velocity was set to 1 m/sec. The drone's flight altitude was optimized to maintain a consistent ground clearance for data accuracy. Figure 5 shows the typical calculation scheme [28,29] for estimating the radius of the maximum exposure area under the drone at the surface (*R1*) and underground (*R2*) as a function of desirable drone altitude (*H*) and requirable target depth (*D*).

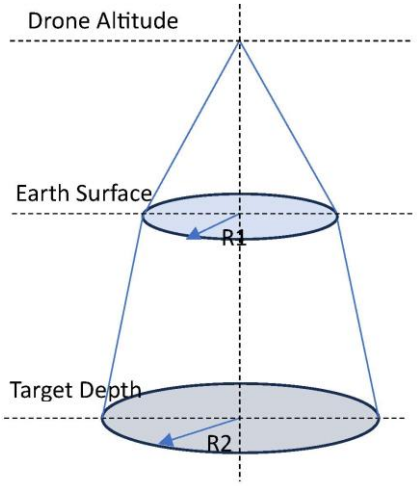

Figure 5. Airborne GPR footprint calculation, modified from [28–31].

Based on Eqs. 1-3, *R1* is a function of the drone's altitude (*H*), speed of the electromagnetic wave in material (v), and radar center frequency (f) [29–31].

$$V = 300/\sqrt{\varepsilon} \quad (1)$$

Preprints (www.preprints.org) | NOT PEER-REVIEWED | Posted: 14 January 2024 doi:10.20944/preprints202401.1034.v1

$$\lambda = V/f \quad (2)$$

$$R1 = \frac{\lambda}{4} + \frac{\sqrt{H \cdot \lambda}}{2} \quad (3)$$

where λ is the wavelength, ε is the value of air relative dielectric permittivity (~1) [26,27]. Eq. 1 returns v_{air} of 300 mm/ns. Based on Eq. 2 and f that was set to 150 MHz, the λ value is 2 m. Therefore, H = 5 m above the ground yields the value of $R1$ equal to ~2 m.

Depth and resolution are also critical factors affecting the quality of data collected through drone-based GPR surveys. Depth refers to how deep the radar waves can penetrate and gather information into the ground. The choice of GPR frequency plays a pivotal role in determining penetration depth. Balancing depth and resolution is an ongoing challenge, and it is essential to strike a harmonious equilibrium to obtain the most informative and high-quality data during drone-based GPR surveys. To estimate the radius $R2$ of the maximum exposure area under the drone at a depth under the earth's surface (Figure 5), and additional parameters such as vertical resolution (D_R) and minimum size (A_{min}) of a detectable object, additional equations are required [28–31]:

$$R2 = R1 + \frac{\sqrt{D \cdot \lambda}}{2} \quad (4)$$

$$D_R = \lambda/2 \quad (5)$$

$$A_{min} = \begin{cases} (D+H)/10, & (D+H)/10 > D_R \\ D_R/2, & (D+H)/10 \leq D_R \end{cases} \quad (6)$$

Considering Children's Park's local clayey saturated soil near-surface lithology, the estimated value ε, according to Eq.1, is ~15 [26,27]. Therefore, following Eq. 2, v_{clay} is 77.46 mm/ns, and hence for the depth D = 15 m, the estimated radius of the object at such a depth $R2$ is ~5 m with D_R = 1 m and A_{min} = 2 m. Empathizing that H = 5 m is a good choice for searching the underground natural rock or soil surface (which is covered by a few meters of distributed clay).

4. Results

The meticulously planned flight path, strategically designed to optimize the capture of subsurface features, is depicted in Figure 4 (green lines with numbers). The drone commenced its survey from the hilltop (the purple circle), where the surface transitions to natural rock, and followed a perpendicular direction to the dip of the hill. The flight was organized into distinct sections to address specific objectives. The initial section, from west to east (waypoints 3 to 8), aimed to circumvent urban obstacles such as 4-meter trees, 1.5-meter fence, and 4.5-meter streetlights while maintaining a low altitude of 5 meters above the ground.

The second section, traversing from northwest to southeast (waypoints 0 to 7), mirrored the first but in the opposite direction, mapping the sub-rock natural surface to the hills' natural surface. The third section was primarily dedicated to examining underground variations in the east-west direction, investigating whether the slope exhibited drastic changes or maintained a consistent formation beneath the surface.

As detailed in Sect. 3, the penetration depth for the aerial survey was established at a minimum of 15 meters underground, a consideration guided by the saturated clay's geophysical properties. This parameter ensured comprehensive subsurface data collection, allowing for a thorough exploration of the geological structure beneath the clayey soil.

Figure 6 presents the radarogram from the first survey section (waypoints 3-8, as illustrated in Figure 4), offering a detailed insight into subsurface structures. The horizontal and vertical axes denote path and depth distances in meters, with the 0-meter level in the vertical direction set at the Children's Park surface. Hilltops are designated in a positive vertical direction, while the subsurface is represented in a negative vertical direction. Waypoints 3-8 are distinctly marked with vertical black lines and corresponding numbers at the top of Figure 6.

Preprints (www.preprints.org) | NOT PEER-REVIEWED | Posted: 14 January 2024 doi:10.20944/preprints202401.1034.v1

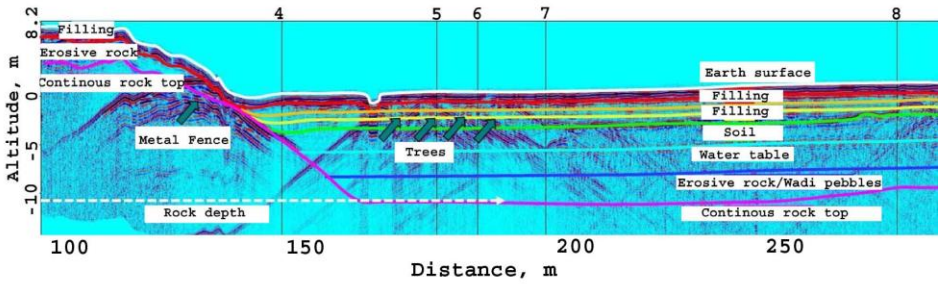

Figure 6. The radargram illustrates the first survey section (waypoints 3-8 from Figure 4). The horizontal and vertical axes represent path and depth distances in meters, with the Children's Park surface at the 0-meter level. Key features include distinct lines representing the surface, variations in distributed soils, a light blue line indicating a water layer at 5 meters depth, a dark blue line marking the top of the weathered rock at around 8 meters depth, and a purple line signifying the natural hard rock surface starting from the hilltop and descending under the park at approximately 10 meters below ground level. Parabolic reflections from obstacles along the flight path are also visible.

The results reveal distinct features in the radargram. The surface is represented by a continuous line (in white), while variations in the distributed soils are marked by red, orange, yellow, and green lines. A light blue line denotes a saturated water layer, validated by the 5-meter depth observed by the drilling campaign (Figure 2). The dark blue line signifies the top of the weathered/erosive rock, positioned approximately 8 meters below the park's surface. A purple line highlights the natural hard rock surface, commencing from the hilltop and descending beneath the park's surface at approximately 10 meters below ground level. Furthermore, hyperbolic reflections of high intensity are evident from fences and trees along the flight path, providing additional insights into the subsurface composition and potential obstacles.

Figure 7 presents radargram from the second and third survey sections (Figure 4, waypoints 0-7 and 7-13 in Figure 7), providing critical insights into the subsurface composition. The color scheme aligns with the description above in Figure 6, with 0 meters set to the park's surface (in white) and a penetration depth of 15 meters underground. Notably, the water layer is identified approximately 4 meters underground, while the desirable rock layer is detected around 8 meters beneath the surface.

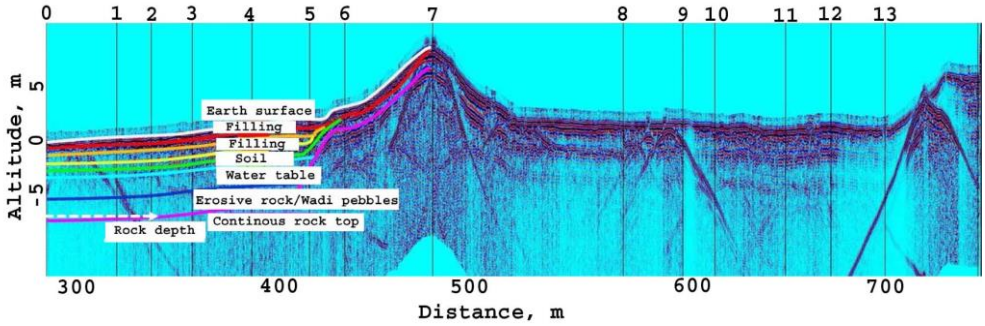

Figure 7. This radargram illustrates the second and third survey sections (waypoints 0-7 and 7-16 from Figure 4). The horizontal and vertical axes represent path and depth distances in meters, with the Children's Park surface at the 0-meter level. Key features include distinct lines representing the surface, variations in distributed soils, a light blue line indicating a water layer at 5 meters depth, a dark blue line marking the top of the weathered rock at around 8 meters depth, and a purple line signifying the natural hard rock surface starting from the hilltop and descending under the park at approximately 10 meters below ground level. Parabolic reflections from obstacles along the flight path are also visible.

Figure 8 provides an updated photo capturing the process of drilling 14-meter pile foundations at the construction site. The pervasive brown, wet, and distributed clayey soil is evident throughout

Preprints (www.preprints.org) | NOT PEER-REVIEWED | Posted: 14 January 2024 doi:10.20944/preprints202401.1034.v1

the image, reflecting the challenges posed by the water table at around 5 meters depth. To counter the risk of collapsing drilling pits, a Bentonite mixture was employed during the drilling process to stabilize the surrounding soil.

Remarkably, the photo unveils the presence of yellow sandstone fragments at the drilling bottom, representing the natural rock layer at an estimated depth of 9 meters beneath the construction site surface. This observation aligns with the subsurface composition revealed in GPR results in Figures 6 and 7. The consistency between the field observation and GPR findings substantiates the accuracy and reliability of the applied aerial GPR technology, showcasing its potential for real-world applications in foundation engineering. Additional hydro-geological analysis of GPR findings showed that they correlated with the natural water flow direction of the park's wadi, descending from east to west.

Figure 8. The photograph of the construction site under study during the pile drilling campaign. Wet brown clayey soil, stabilized with Bentonite, is visible on the surface. Extracted yellow sandstone at 9 meters corresponds accurately to GPR findings (Figures 6 and 7), affirming the reliability of aerial GPR for subsurface mapping in foundation engineering.

4. Discussion

Our study demonstrates the remarkable advantage of drone-based ground penetrating radar (GPR) in accurately mapping the natural rock surface beneath a substantial layer of clayey soil at the construction site in Beer-Sheva's Children's Park. The conventional challenges faced by traditional surveying methods, such as spot-wise borehole drilling, were overcome by leveraging the unique capabilities of drone-based GPR. Combining aerial platforms with subsurface sensing capabilities enabled a comprehensive understanding of the complex subsurface structure, which was crucial for foundation engineering. Our choice of a 150 MHz central frequency is a successful compromise between the clay dielectric properties, which proved effective in penetrating the clayey soil and revealing the underlying natural rock formations. Especially using an unshielded low-frequency dipole antenna, generally not recommended in urban environments due to the effect of above-ground obstacles (e.g., fence, trees, etc., Figure 6), allowed us to distinguish natural subsurface features (Figures 6,7) successfully.

The flight path planning, illustrated in Figures 4, 6, and 7, strategically considered urban obstacles like trees, fences, and streetlights, allowing the drone to navigate efficiently at a low altitude of 5 meters above the ground. This meticulous planning, coupled with the high-resolution GPR data, enabled the precise identification of the transition from clay to natural rock surfaces. The validation process, involving the validation of the drilling results, geological maps, and on-site observations during foundation drilling, consistently affirmed the accuracy of our GPR-based mapping. The success in differentiating soil types and identifying the natural rock surface at varying depths

showcases the potential of drone-based GPR as a transformative tool in subsurface characterization for foundation engineering applications.

The successful correlation between the GPR observations and the actual subsurface structure validates the technology's efficacy and underscores its significance in overcoming challenges associated with waterlogged clayey soil during construction activities.

The insights provided by the radargram compensate for the limitations encountered during the drilling test, offering valuable data for informed decision-making in construction planning. Moreover, it is invaluable in ensuring foundation structures' stability and effectiveness in varying geological conditions. This information is crucial for engineering considerations, aiding in planning appropriate foundation pile lengths for future structures.

5. Conclusions

The application of drone-based GPR was an effective tool in identifying the boundaries between disturbed clay soil and rock formations along the old Wadi stream. The methodology of its application in generally unfavorable conditions, clayey soil, and above-ground obstacles (trees, metal fence, etc.) was considered. The potential of using unmanned ground penetrating radar (GPR) equipped with an unshielded dipole antenna as a transformative tool in geospatial analysis has been successfully demonstrated. The study contributes to understanding drone-based ground penetrating radar technology for mapping disturbed soil boundaries as an integral part of foundation design in complex environments.

The features of integration of ground-based and drone-based GPR technologies and the possibility of studying horizontal and vertical engineering objects are the issues for our future studies.

Author Contributions: Conceptualization, M.F., and VF.; methodology, MF., and VF.; software, MF.; validation, M.F., and V.F.; formal analysis, M.F.; investigation, M.F., and V.F; resources, V.F.; data curation, V.F.; writing—original draft preparation, M.F. and V.F.; writing—review and editing, M.F. and V.F.; visualization, M.F.; supervision, V.F.; project administration, M.F. All authors have read and agreed to the published version of the manuscript.

Funding: VF acknowledges the support from the European Union's Horizon 2020 research and innovation program under the Marie Sklodowska-Curie RISE project EffectFact, grant agreement no. 101008140.

Data Availability Statement: All data generated and analyzed during this study are included in the article.

Conflicts of Interest: The authors declare no conflict of interest.

References

1. Šepac, Z. Foundation engineering structure. In 7th International Conference on Road and Rail Infrastructure. **2022**.
2. Ngo, V. L.; Lee, C.; Kim, J.M. Effects of stratification on soil–foundation–structure interaction: centrifugal observation and numerical simulation. *Applied Sciences*, **2021**, *11(2)*, 623.
3. Patil, N. N.; Rajashekar Swamy, H. M.; Shivashankar, R. Effect of Reinforced Soil–Structure Interaction on Foundation Settlement Characteristics of a Three-Dimensional Structure. In Innovations in Soft Computing and Information Technology: Proceedings of ICEMIT 2017, **2019**, *3*, 135-161. Springer Singapore.
4. Sass, O.; Friedmann, A.; Haselwanter, G.; Wetzel, K.-F. Investigating thickness and internal structure of alpine mires using conventional and geophysical techniques. *Catena* **2010**, *80*, 195–203.
5. Algeo, J.; Van Dam, R.L.; Slater, L. Early-Time GPR: A Method to Monitor Spatial Variations in Soil Water Content during Irrigation in Clay Soils. *Vadose Zone J.* **2016**. doi:10.2136/vzj2016.03.0026.
6. Cheng, Q.; Su, Q.; Binley, A.; Liu, J.; Zhang, Z.; Chen, X. Estimation of surface soil moisture by a multi-elevation UAV-based ground penetrating radar. *Water Resources Research*, **2023**, *59*, e2022WR032621. https://doi.org/10.1029/2022WR032621.
7. Guo, W.; Dong, C.; Lin, C.; Zhang, T.; Zhao, Z.; Li, J. 3D Sedimentary Architecture of Sandy Braided River, Based on Outcrop, Unmanned Aerial Vehicle and Ground Penetrating Radar Data. *Minerals* **2022**, *12*, 739. https://doi.org/10.3390/min12060739

8. Pueyo-Anchuela, Ó.; Pocoví Juan, A.; Soriano, M.A.; Casas-Sainz, A.M. Characterization of karst hazards from the perspective of the doline triangle using GPR — Examples from Central Ebro Basin (Spain). *Engineering Geology* **2009**, *108*, 225–236.
9. Bekić, G. Railroad survey application, Application notes, www.geoscanners.com (downloaded on 05.03.2015).
10. Kovacevic, M.S.; Gavin, K.; Stipanovic Oslakovic, I.; Bacic, M. A new methodology for assessment of railway infrastructure condition. 6th Transport Research Arena April 18-21, 2016. *Transportation Research Procedia* **2016**, *14*, 1930 – 1939.
11. Frid A.; Frid, V. 2023. Moisture effect on asphalt dielectric permittivity: simulating, sensitivity analysis, and experimental validation. *International Journal of Pavement Research and Technology*. https://doi.org/10.1007/s42947-023-00282-2.
12. Zayed, T.; Dawood, T.; Abouhamad, M.; Alsharqawi, M. Special Issue "Ground Penetrating Radar (GPR) Applications in Civil Infrastructure Systems". *Remote Sens*. **2022**, *14*, 5682. https://doi.org/10.3390/rs14225682
13. Altdorff, D.; Schliffke, N.; Riedel, M.; Schmidt, V., van der Kruk, J.; Vereecken, H.; Becken, M. UAV-borne electromagnetic induction and ground-penetrating radar measurements: a feasibility test. *Water Resour. Res* **2014**, *42*, W11403.
14. Eröss, R.; Stoll, J. B.; Bergers, R.; Tezkan, B. Three-component VLF using an unmanned aerial system as sensor platform. *First Break* **2013**, *31(7)*.
15. Booth, A. D.; Koylass, T. M. Drone-mounted ground-penetrating radar surveying: Flight-height considerations for diffraction-based velocity analysis. *Geophysics* **2022**, *87(4)*, WB69-WB79.
16. Shin, Y.H.; Shin, S.Y.; Rastiveis, H.; Cheng, Y.T.; Zhou, T.; Liu, J.; Habib, A. UAV-Based Remote Sensing for Detection and Visualization of Partially-Exposed Underground Structures in Complex Archaeological Sites. *Remote Sensing* **2023**, *15(7)*, 1876.
17. Wu, S.; Wang, L.; Zeng, X.' Wang, F.; Liang, Z.; Ye, H. UAV-Mounted GPR for Object Detection Based on Cross-Correlation Background Subtraction Method. *Remote Sensing* **2022**, *14(20)*, 5132.
18. Wu, K.; Rodriguez, G.A.; Zajc, M.; Jacquemin, E.; Clément, M.; De Coster, A.; Lambot, S. A new drone-borne GPR for soil moisture mapping. *Remote Sensing of Environment* 2019, *235*, 111456.
19. Wu, K.; Lambot, S. 2022 Analysis of Low-Frequency Drone-Borne GPR for Root-Zone Soil Electrical Conductivity Characterization. *IEEE Transactions on Geoscience and Remote Sensing* **2022**, *60*, 2006213. DOI: 10.1109/TGRS.2022.3198431.
20. Ruols, B.; Baron, L.; Irving, J. High-density 3D and 4D GPR data acquisitions over alpine glaciers using a newly developed drone-based system (No. EGU23-9619). Copernicus Meetings. **2023**.
21. Vergnano, A.; Franco, D.; Godio, A. Drone-Borne GroundPenetrating Radar for Snow Cover Mapping. *Remote Sens.* **2022**, *14*, 1763. https://doi.org/10.3390/rs14071763
22. Saponaro, A.; Dipierro, G.; Cannella, E.; Panarese, A.; Galiano, A.M.; Massaro, A. A UAV-GPR Fusion Approach for the Characterization of a Quarry Excavation Area in Falconara Albanese, Southern Italy. *Drones* **2021**, *5*, 40. https://doi.org/10.3390/drones5020040.
23. Edemsky, D.; Popov, A.; Prokopovich, I.; Garbatsevich, V. Airborne ground penetrating radar, field test. *Remote Sensing* **2021**, *13(4)*, 667.
24. ASTM D 2487 – 00, Standard Practice for Classification of Soils for Engineering Purposes (Unified Soil Classification System). Approved March 10, 2000. Published May **2000**. ASTM International, 100 Barr Harbor Drive, PO Box C700, West Conshohocken, PA 19428-2959, United States.
25. Zilberman, E. Geological Map of Israel, Beer Sheva, Sheet 14-IV, 1:50,000; Israel Geological Survey: Jerusalem, Israel, **2018**.
26. Annan, A.P. Electromagnetic principles of ground penetrating radar. In Ground Penetrating Radar: Theory and Applications. Ed. Jol H.M. **2009**. Elsevier Science, Radarweg 29, PO Box 211, 1000 AE Amsterdam, The Netherlands The Boulevard, Langford Lane, Kidlington, Oxford OX5 1GB, UK.
27. Daniels, D. Ground Penetrating Radar. **2004**. The Institute of Electrical Engineers. London UK.
28. Huisman, J.A.; Hubbard, S.S.; Redman, J.D.; Annan, A. P. Measuring soil water content with ground penetrating radar: A review. *Vadose Zone Journal* **2003**, *2(4)*, 476–491. https://doi.org/10.2113/2.4.476.
29. Cheng, Q.; Su, Q.; Binley, A.; Liu, J.; Zhang, Z.; Chen, X. Estimation of surface soil moisture by a multi-elevation UAV-based ground penetrating radar.
30. *Water Resources Research* **2023**, *59*, e2022WR032621. https://doi.org/10.1029/2022WR032621https://www.xyht.com/aerialuas/gpr-on-a-drone/
31. Emilsson, J.; Friborg, J.; Gustafsson, J.; Adcock, J.; Viberg, A. On the Development and Application of Airborne GPR Solutions *First Break* **2022**, *40(8)*, 47 – 54.

 doi:10.20944/preprints202401.1034.v1

disclaim responsibility for any injury to people or property resulting from any ideas, methods, instructions or products referred to in the content.